

The evolution of the rest-frame J - and H -band luminosity function of galaxies to $z = 3.5$

Mauro Stefanon^{1*} and Danilo Marchesini²

¹*Observatori Astronòmic Universitat de València, C/ Catedrático Agustín Escardino Benlloch, 7, 46980, Valencia, Spain*

²*Tufts University, Robinson Hall, 212 College Avenue, Medford, MA 02155, USA*

Accepted –. Received –; in original form –

ABSTRACT

We present the rest-frame J - and H - band luminosity function (LF) of field galaxies, based on a deep multi-wavelength composite sample from the MUSYC, FIRES and FIREWORKS survey public catalogues, covering a total area of 450 arcmin². The availability of flux measurements in the Spitzer IRAC 3.6, 4.5, 5.8, and 8 μ m channels allows us to compute absolute magnitudes in the rest-frame J and H bands up to $z = 3.5$ minimizing the dependence on the stellar evolution models. We compute the LF in the four redshift bins $1.5 < z < 2.0$, $2.0 < z < 2.5$, $2.5 < z < 3.0$ and $3.0 < z < 3.5$. Combining our results with those already available at lower redshifts, we find that (1) the faint end slope is consistent with being constant up to $z = 3.5$, with $\alpha = -1.05 \pm 0.03$ for the rest-frame J band and $\alpha = -1.15 \pm 0.02$ for the rest-frame H band; (2) the normalization ϕ^* decreases by a factor of 4-6 between $z = 0$ and $z \simeq 1.75$ and by a factor of 2-3 between $z \simeq 1.75$ and $z = 3.25$; (3) the characteristic magnitude M^* shows a brightening from $z = 0$ to $z \simeq 2$ followed by a slow dimming to $z = 3.25$. We finally compute the luminosity density (LD) in both rest-frame J and H bands. The analysis of our results together with those available in the literature shows that the LD is approximately constant up to $z \approx 1$, and it then decreases by a factor of 6 up to $z = 3.5$.

Key words: galaxies: evolution – galaxies: statistics – galaxies: high-redshift – galaxies: luminosity function, mass function – infrared: galaxies

1 INTRODUCTION

In the current concordance model, galaxies are the result of continuous mergers of dark matter halos driving baryonic matter assembly. In the last decades, simulations on halo occupation models have been able to quite accurately plot the formation of dark matter clusters. However, big uncertainties still remain at the time of translating dark matter haloes to what can actually be detected with our telescopes.

To this respect, the luminosity function (LF) of galaxies, i.e. the number density of galaxies per unit flux, is an extremely powerful tool to study the galaxy population and its evolution with cosmic time. Specifically, the analysis of the LF at different rest-frame wavelengths can give us information on different aspects of our present view of the Universe. The UV-optical LF allows for the study of the content and the evolution of the star formation rates with cosmic time. On the other hand the near infra-red (NIR) LF, being less sensitive to the absorption by dust and dominated by the light of older stars, is a better estimator of the overall stellar mass assembly of galaxies and of its rate of growth with time, revealing itself as a good test-bench for halo models.

The local NIR LF is still not yet well determined. Although a number of measurements have been derived so far, there seems to be uncertainties especially for the faint end slope α . Estimates of the slope α range from ≈ -0.8 (Bell et al. 2003; Eke et al. 2005), to $\alpha \approx -1.2$ (Jones et al. 2006), with a median value around -1 (Mobasher, Sharples, & Ellis 1993; Glazebrook et al. 1995; Cowie et al. 1996; Gardner et al. 1997 and Szokoly et al. 1998; Kochanek et al. 2001; Cole et al. 2001 and Hill et al. 2010).

At even larger redshift, the LF determinations (most of which are done in the rest-frame K_S band) still suffer from significant uncertainties (Saracco et al. 2006). The faint-end slope seems to be always compatible with $\alpha = -1$ (Drory et al. 2003; Pozzetti et al. 2003; Dahlen et al. 2005; Saracco et al. 2006; Cirasuolo et al. 2010) although these measurements suffer from the large uncertainties given by the limits in the depth of the photometric catalogues available so far. There seems to be a general consensus however that the NIR LF does not significantly evolve to $z \approx 1$ with respect to the local LF (Cowie et al. 1996; Pozzetti et al. 2003; Drory et al. 2003; Feulner et al. 2003; Dahlen et al. 2005). A brightening of the characteristic magnitude is instead found around $z \approx 1.2 - 1.5$ together with a decrease of the normalization, decrease that is seen up to $z = 3$ (Saracco et al. 2006; Cirasuolo et al. 2010).

* E-mail: mauro.stefanon@uv.es

In this paper we present the rest-frame J - and H -bands LFs and luminosity density (LD) of field galaxies, obtained from three deep photometric redshift surveys, namely MUSYC, FIRES and FIREWORKS, complemented by deep *Spitzer* 3.6, 4.5, 5.8, and 8 μm data. As discussed in e. g. Berta et al. (2007), the combination of the Planck spectral peak from low-mass stars, the minimum in the H^- opacity in stellar atmospheres and the molecular absorptions in the spectra of cold stars produce a maximum for the emission in the rest-frame NIR portion of galaxy spectra located at 1.6 μm (the so called 1.6 μm bump). Furthermore, the AGN light can contribute significantly to the rest-frame K band. Specifically, the contribution from the dust torus of the AGN can be in the rest-frame K band a factor of 10 larger than in the rest-frame J band, and a factor of 4 larger than in the rest-frame H band (e.g., Polletta et al. 2008). The adoption of the rest-frame J and H bands makes thus the measurement of the LFs and LDs less sensitive to potential dust-obscured AGN contamination compared to measurements of the LFs in the rest-frame K_s , yet allowing us to sample a wavelength range dominated by stellar emission and very little affected by obscuration by dust. The combination of depth and wavelength coverage in the mid-IR out to 8 μm allows us to directly probe the rest-frame J and H bands out to $z \simeq 3.5$, relying more on observational data rather than on stellar population models, which are still significantly uncertain in the rest-frame NIR, due to different implementations of the TP-AGB phase (Maraston 2005; Conroy, Gunn, & White 2009). The total surveyed area sums to 450 arcmin^2 with complete U-to-8 μm coverage, reducing thus the effects of cosmic variance, which we estimate to give on average a 15-20% contribution.

This paper is organized as follows. In section 2 we present the data sets used for this work together with a description on how we recover photometric redshifts and we select galaxies from the full sample. Section 3 presents the three methods adopted to estimate the LF and its associated uncertainties. In section 4 we present our results, while our conclusions are summarized in section 5.

Throughout this work, the adopted cosmology is $\Omega_\Lambda = 0.7$, $\Omega_m = 0.3$ and $H_0 = 70 \text{ Km/s/Mpc}$. All magnitudes are expressed in the AB system.

2 THE SAMPLE

For this work we used a total of seven public K_s -selected catalogues coming from three different deep multi-wavelength galaxy surveys covering the range from the optical to the Spitzer IRAC 8 μm waveband: the MULTI-wavelength Survey by Yale-Chile (MUSYC - Marchesini et al. 2009), the Faint InfraRed Extragalactic Survey (FIRES - Labbè et al. 2003, Forster Schreiber et al. 2006) and the GOODS Chandra Deep Field-South (FIREWORKS - Wuyts et al. 2008). Although they have all been presented in Marchesini et al. (2009), for readers' sake these surveys will be briefly described in the following sections.

2.1 MUSYC

The deep NIR MUSYC survey consists of four $10' \times 10'$ fields, namely, Hubble Deep Field-South 1 and 2 (HDFS-1, HDFS-2, hereafter), the SDSS-1030 field, and the CW-1255 field, observed with the Infrared Side Port Imager (ISPI) camera at the Cerro Tololo Inter-American Observatory (CTIO) Blanco 4 m telescope, for a total surveyed area of 430 arcmin^2 . A complete description of the deep NIR MUSYC observations, reduction procedures, and the

construction of the K -selected catalog with U -to- K photometry is presented in Quadri et al. (2007). Deep Spitzer-IRAC 3.6-8.0 μm imaging is also available for the four fields. The average total limiting magnitudes of the IRAC images are 24.5, 24.2, 22.4, and 22.3 (3σ , AB magnitude) in the 3.6, 4.5, 5.8, and 8.0 μm bands, respectively. The K -selected catalogs with IRAC photometry included is publicly available at <http://www.astro.yale.edu/musyc>. The SDSS-1030, CW-1255, HDFS-1, and HDFS-2 catalogs are K_s band-limited multicolor source catalogs down to $K_{s,tot} = 23.6, 23.4, 23.7, \text{ and } 23.2$, for a total of 3273, 2445, 2996, and 2118 sources, over fields of 109, 105, 109, 106 arcmin^2 , respectively. All four fields were exposed in 14 different bands, U, B, V, R, I, z, J, H, K, and the four IRAC channels. The SDSS-1030, CW-1255, HDFS-1, and HDFS-2 K -selected catalogs have 90% completeness levels at $K_{s,90} = 23.2, 22.8, 23.0, \text{ and } 22.7$, respectively. The final catalogs used in the construction of the composite sample have 2825, 2197, 2266, and 1749 objects brighter than the 90% completeness in the K_s band, over an effective area of 98.2, 91.0, 97.6, and 85.9 arcmin^2 , respectively, for a total of 9037 sources over 372.7 arcmin^2 .

2.2 FIRES

FIRES consists of two fields, namely, the Hubble Deep Field-South proper (HDF-S) and the field around MS 1054-03, a foreground cluster at $z = 0.83$. A complete description of the FIRES observations, reduction procedures, and the construction of photometric catalogs is presented in detail in Labbè et al. (2003) and Forster Schreiber et al. (2006) for HDF-S and MS 1054-03 (hereafter HDFS and MS-1054), respectively. Both K_s -selected catalogs were later augmented with Spitzer-IRAC data (Wuyts et al. 2007; Toft et al. 2007)). The HDFS catalog has 833 sources down to $K_{s,tot} = 26.0$ over an area of $2.5 \times 2.5 \text{ arcmin}^2$. The MS-1054 catalog has 1858 sources down to $K_{s,tot} = 25.0$ over an area of $5.5 \times 5.3 \text{ arcmin}^2$. The HDFS field was exposed in the WFPC2 U300, B450, V606, I814 passbands, the ISAAC J_s , H, and K_s bands, and the four IRAC channels. The MS-1054 K_s -selected catalog comprises FORS1 U, B, V, WFPC2 V606 and I814, ISAAC J_s , H, and K_s , and IRAC 3.6-8.0 μm photometry. The HDFS and MS-1054 catalogs have 90% completeness levels at $K_{s,90} = 25.5$ and 24.1, respectively. The final HDFS and MS-1054 catalogs used in the construction of the composite sample have 715 and 1547 objects brighter than the 90% completeness in the K_s band, over an effective area of 4.5 and 21.0 arcmin^2 , respectively.

2.3 FIREWORKS

In this work, we adopted the K_s -selected catalog (dubbed FIREWORKS) of the CDFS field constructed based on the publicly available GOODS-CDFS data by Wuyts et al. (2008). The photometry was performed in an identical way to that of the FIRES fields, and the included passbands are the ACS B435, V606, i775, and z850 bands, the WFI U38, B, V, R, and I bands, the ISAAC J, H, and K_s bands, and the four IRAC channels. The K_s -selected catalog comprises 6308 objects down to $K_{s,tot} = 24.6$ over a total surveyed area of 138 arcmin^2 ; the variation in exposure time and observing conditions between the different ISAAC pointings lead to an inhomogeneous depth over the whole GOODS-CDFS field (hereafter CDFS). The final CDFS catalog used in the construction of the composite sample comprises 3559 objects brighter than the 90% completeness level ($K_{s,90} = 23.7$), over an effective area of 113 arcmin^2 with coverage in all bands.

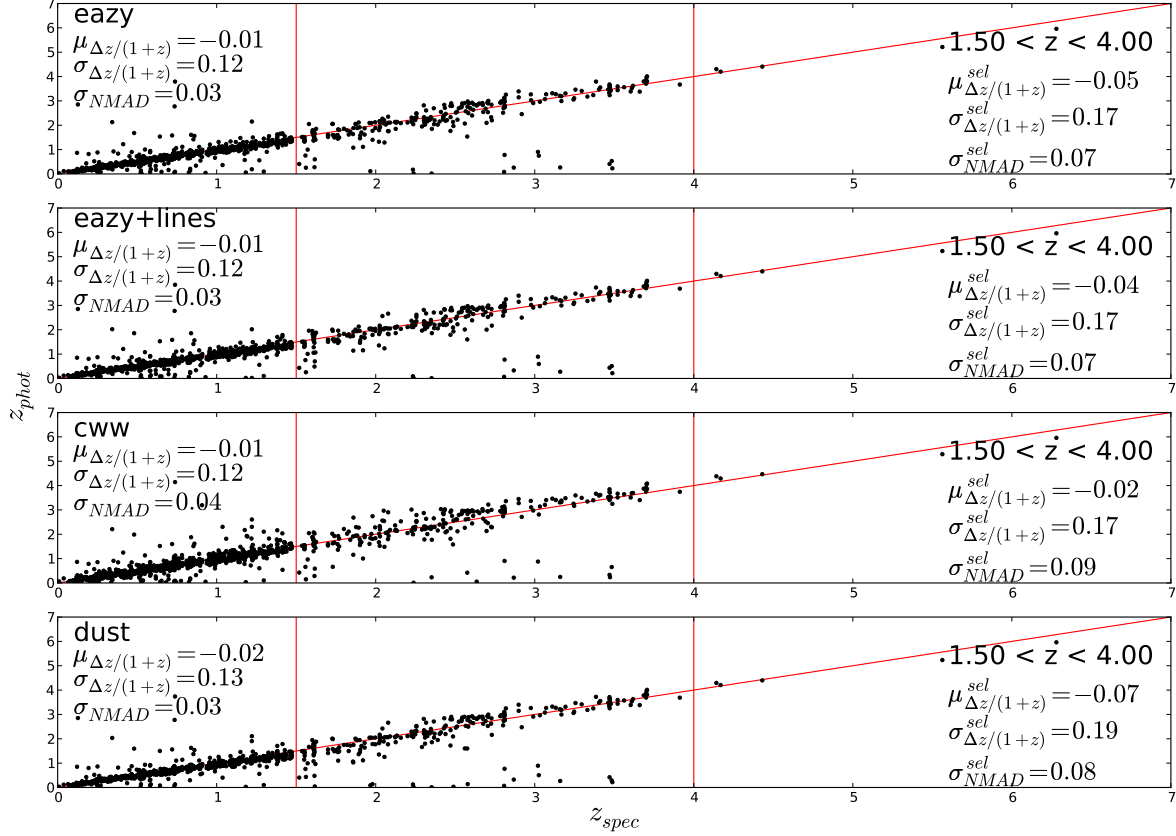


Figure 1. Photometric redshifts compared to spectroscopic redshifts, for the four different SED sets. From top to bottom: EAZY default template set; EAZY default template set with the addition of $\text{Ly}\alpha$, $\text{H}\alpha$, $\text{H}\beta$, $[\text{OII}]$ and $[\text{OIII}]$ emission lines; Coleman, Wu and Weedman template set and EAZY SED set with dusty galaxy template (see text for details). $\mu_{\Delta z/(1+z)}$ and $\sigma_{\Delta z/(1+z)}$ are the average and the standard deviation of $\Delta z/(1+z)$, respectively; σ_{NMAD} is the normalized median absolute deviation.

2.4 Photometric redshift and star/galaxy separation

The downloaded catalogues all come with photometric redshift information; spectroscopic redshifts are also available for a small fraction of galaxies (around 10% of the whole sample). However, we re-computed photometric redshifts, using the publicly available EAZY code (Brammer et al. 2008), and adopting four different sets of Spectral Energy Distribution (SED) templates. The first SED set is the EAZY default template set; it consists of 5 SED templates built on the base of PEGASE models (Fioc & Rocca-Volmerange 2006), reproducing the colors of galaxies in the semi-analytic models by De Lucia & Blaizot (2007), plus a template representing a 50 My galaxy with heavy dust obscuration. The second set is composed by a modified version of the standard EAZY templates, with the addition of $\text{Ly}\alpha$, $\text{H}\alpha$, $\text{H}\beta$, $[\text{OII}]$ and $[\text{OIII}]$ emission lines. The third is a set of six templates based on Coleman, Wu, & Weedman (1980) colors, included in the Bayesian Photometric Redshift code (BPZ - Benítez 2000). The last set is an extension of the standard EAZY template set with the inclusion of a 1Gyr galaxy template, with $\tau = 100$ Myr and $A_V = 3$ mag, similar to the reddest template used in Blanton & Roweis (2007).

For all the four cases, the same default template error function and K -band prior was adopted.

Figure 1 shows the z_{spec} vs. z_{phot} plot for the four SED template sets used. The average $\Delta z/(1+z)$ are respectively -0.01, -0.01, -0.01, and -0.02 for the EAZY, EAZY+lines, CWW and EAZY+dust template sets when considering the full sample, and -0.05, -0.04, -0.02, and -0.07 when computed on the redshift range $1.5 < z < 4.0$. The standard deviations $\sigma_{\Delta z/(1+z)}$ are 0.12, 0.12, 0.12, and 0.13 respectively for the full sample and 0.17, 0.17, 0.17, and 0.19 in the redshift interval $1.5 < z < 4.0$. The normalized median absolute deviation, σ_{NMAD} ¹, is 0.03, 0.03, 0.04, and 0.03 over the whole redshift range, and 0.07, 0.07, 0.09, and 0.08 in the redshift interval $1.5 < z < 4.0$. The fraction of catastrophic photometric redshift ($n(\frac{\Delta z}{1+z}) > 5\sigma$) is 0.042, 0.046, 0.045 and 0.048 respectively.

We finally chose to adopt the standard EAZY template set, which is the one presenting the smallest deviation between spectroscopic and photometric redshifts in the targeted redshift range.

The separation between stars and galaxy was done with the

¹ The normalized median absolute deviation σ_{NMAD} , defined as $1.48 \times \text{median}[|(\Delta z - \text{median}(\Delta z))/(1+z)|]$, is equal to the standard deviation for a Gaussian distribution, and it is less sensitive to outliers than the usual definition of the standard deviation (e.g., Ilbert et al. 2006).

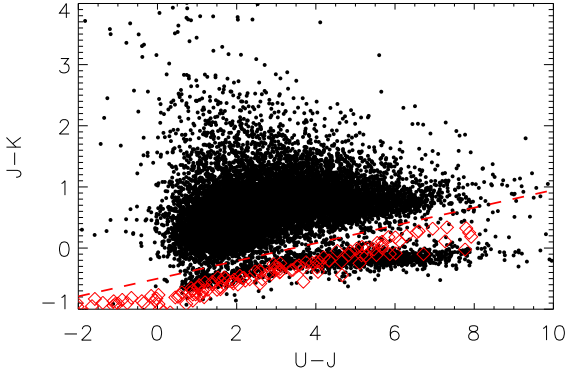


Figure 2. Two colours diagram for all the sources in the composite catalogues. Colours from Pickles (1998) stellar atmosphere models are shown as red diamonds. The red dashed line represents Eq. 1, which we adopted to separate stars from galaxies

colour-colour diagram ($U - J$) vs. ($J - K_s$) (see figure 2). The same colours were also computed from the Pickles (1998) stellar atmosphere models, in order to improve the boundaries between stars and galaxy, especially for the reddest stars which fall out of the main sequence (see figure 2 for full details).

Galaxies were selected among the object satisfying the relation:

$$(J - K_s) \geq 0.145 \cdot (U - J) - 0.45 \quad (1)$$

As a cross-check, we run the EAZY code with the Pickles (1998) model stellar atmosphere and checked that the objects identified as galaxies via the two-colour diagram had a χ^2 greater than the χ^2 obtained on the same object with the EAZY galaxy template set. This criteria was satisfied by all objects previously selected as galaxies with only 6.5% of the objects selected as stars showing a discordant value for the χ^2 , giving confidence in our method to separate stars from galaxies.

A star-galaxy separation was also available in the original FIRES and FIREWORKS public catalogues. This selection was based on spectroscopy, SED-fitting with stellar templates and visual inspection of the object morphology (Rudnick et al. 2006, 2003). We verified that those objects selected as stars in the FIRES catalogue were actually falling in the correct region of our two-colour plot.

The availability of *Spitzer* IRAC data for all our sample allows us to compute absolute magnitudes in the rest-frame J and H bands with little dependance on the SED templates; in fact, as an extreme case, the rest-frame H band at $z = 3.5$ is shifted to the range $6.7-7.9\mu\text{m}$, well bracketed by the *IRAC* channels 3 and 4, centered at 5.8 and $8\mu\text{m}$.

Our final catalogue is composed by a total of 14295 galaxies, with redshifts determinations to $z = 6.2$ and median redshift $z_{\text{med}} \simeq 1$, distributed over an effective area of 450 arcmin^2 . In the redshift range of interest, $1.5 < z < 3.5$, there is a total of 3496 objects, of which $\approx 6\%$ have spectroscopic redshifts.

3 METHODOLOGY

For the measurement of the LF, we adopted three among the most widely used methods, namely the $1/V_{\text{max}}$ (Schmidt 1968), the

STY maximum likelihood (Sandage, Tammann, & Yahil 1979) and the Step-Wise Maximum Likelihood (Efsthathiou, Ellis, & Peterson 1988).

The need to analyze composite samples with different photometric depth was overcome by applying standard techniques available for each chosen method. Below we summarize them.

3.1 $1/V_{\text{max}}$

The $1/V_{\text{max}}$ method, first introduced by Schmidt (1968), was then generalized by Avni & Bahcall (1980) to allow the simultaneous analysis of composite samples. This method presents a number of advantages: it is simple to code, it directly estimates the normalization of the LF, and it does not make any assumption on the spatial distribution of galaxies. The draw-back is that it is sensitive to the presence of clustering in the sample, affecting the estimate of the faint end.

In a given redshift interval $[z_1, z_2]$, the galaxy number density per unit magnitude in the k -th absolute magnitude bin $\Phi_k(M)$ is computed as follows:

$$\Phi_k(M) = \frac{1}{\Delta M} \sum_{i=1}^{N_{\text{gal}}} \frac{1}{V_{\text{max},i}} \quad (2)$$

where ΔM is the width of the magnitude bin and N_{gal} is the number of galaxies in the redshift interval of interest. In the *coherent* analysis proposed by Avni & Bahcall (1980), $V_{\text{max},i}$ is given by:

$$V_{\text{max},i} = \sum_{j=1}^{n_s} \Omega_j \int_{z_1}^{\min(z_2, z_{\text{max},i,j})} \frac{dV}{dz} dz \quad (3)$$

with n_s the number of samples constituting the full catalogue, Ω_j the apparent area in steradians corresponding the the j -th sample, dV/dz the co-moving volume element per steradian and $z_{\text{max},i,j}$ the maximum redshift at which the i -th galaxy could have been observed within the flux limit of the j -th sample. Standard Poisson errors were associated to each $\Phi_k(M)$.

3.2 Step-wise maximum likelihood

This method, developed by Efsthathiou, Ellis, & Peterson (1988), is based on a maximum likelihood estimate and with a non-parametric form. This method relies on the fact that the number density of galaxies $\Phi(M, \mathbf{x})$ can be factorized into a function which depends on luminosity only, $\phi(M)$, and a factor depending on the position $f(\mathbf{x})$ so that $\Phi(M, \mathbf{x}) = \phi(M) \cdot f(\mathbf{x})$. In particular, this means that the normalization factor of Φ is lost during the maximization of the likelihood, and should then be determined in some other way. The LF $\Phi(M)$ is expressed as the sum over n steps as:

$$\Phi(M) = \phi_i, M_i - \Delta M/2 < M < M_i + \Delta M/2, i = 1, \dots, n \quad (4)$$

By minimizing the natural logarithm of the likelihood expression, a recursive formula is found, allowing to compute the ϕ_i . In order to take into account the non uniform magnitude limits of our data sets, we adopted the modification of the recursive expression as presented in Hill et al. (2010):

$$\phi_i \Delta M = \frac{\sum_{k=1}^{N_{\text{gal}}} W(M_i - M_k)}{\sum_{k=1}^{N_{\text{gal}}} \left[H(M_i - M_{f,k}) / \sum_{j=1}^{N_{\text{gal}}} \phi_j \Delta M H(M_j - M_{f,k}) \right]}$$

where W is a *window* function:

$$W(x) = \begin{cases} 1 & \text{if } -\Delta M/2 < x \leq \Delta M/2 \\ 0 & \text{otherwise} \end{cases} \quad (5)$$

and

$$H(x) = \begin{cases} 1 & \text{if } x \leq -\Delta M/2 \\ 1/2 - x/\Delta M & \text{if } -\Delta M/2 < x \leq \Delta M/2 \\ 0 & \text{otherwise} \end{cases} \quad (6)$$

Uncertainties were computed by taking the square root of the first n diagonal elements of the inverse of the information matrix (see Efstathiou, Ellis, & Peterson 1988).

The SWML method does not compute the normalization itself. For it, we rescaled the LF shape by applying the conservation of the number of galaxies and using the information from the $1/V_{max}$ method, as in Hill et al. (2010). Specifically, given an absolute magnitude range, let N be the number of galaxies included in the given magnitude interval. The redshift edges allowing the selected sub-sample to be observed are then computed, together with the associated maximum co-moving volume V_{max} . The number density of galaxies obtained from the SWML estimate is then rescaled in order to match the N/V_{max} value. The above method can thus be considered as a $1/V_{max}$ LF computed on a single wide absolute magnitude bin.

3.3 STY maximum likelihood

The third technique employed to compute the LF is the parametric method of Sandage, Tammann, & Yahil (1979). The advantage is that the resulting LF is not binned, but instead it is a continuous function. On the other side, the shape of the LF is constrained by the model adopted. Similarly to the SWML, the STYML assumes that the LF can be separated into a term depending on the spatial distribution and a term which depends on the luminosity distribution, thus losing the normalization.

The expression for the probability p_i of seeing galaxy i in the sample can be written as:

$$p \propto \frac{\phi_i(M)}{\int_{M_f(m_s)}^{M_b(m_s)} \phi(M) dM} \quad (7)$$

where the explicit dependence of the bright and faint absolute magnitude limits M_b and M_f to the apparent magnitude m_s of the original catalogue allows to take into account the non uniform photometric depth across the seven catalogues constituting the final sample.

The $\phi(M)$ function was chosen to follow the Schechter (1976) distribution:

$$\phi(M) = (0.4 \ln 10) \phi^* 10^{0.4(M^* - M)(1+\alpha)} \exp \left[-10^{0.4(M^* - M)} \right] \quad (8)$$

where ϕ^* is the normalization, α is the faint-end slope, and M^* is the characteristic magnitude indicating the change from the power-law to the exponential regime. The normalization factor ϕ^* was obtained by imposing the conservation of the number of galaxies in the total sample.

Confidence levels for α and M^* corresponding to 68%, 95% and 99% were computed from the ellipsoid of parameters defined by:

$$\ln \mathcal{L} = \ln \mathcal{L}_{max} - 0.5 \chi^2_{\beta}(N) \quad (9)$$

where \mathcal{L} is the maximum likelihood function and \mathcal{L}_{max} its value at maximum, while $\chi^2_{\beta}(N)$ is the β -point of the χ^2 distribution with N degrees of freedom (Efstathiou, Ellis, & Peterson 1988). Uncertainties on the normalization factor ϕ^* were computed from the

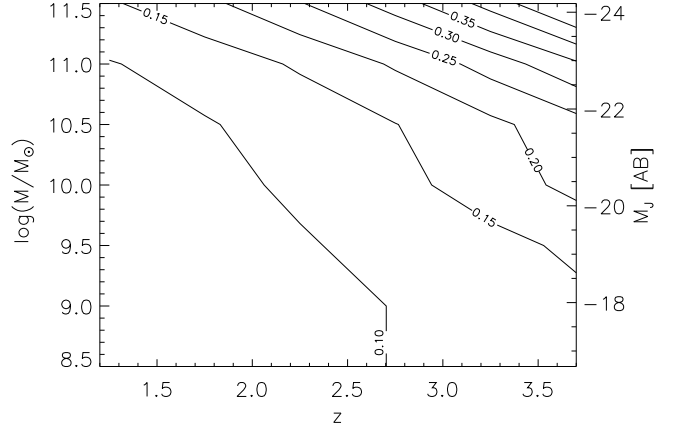


Figure 3. Cosmic variance estimate for our survey geometry following Moster et al. (2010), as a function of redshift and mass (left vertical axis) and absolute magnitude (right vertical axis).

range of values compatible with the 1σ uncertainties in the α and M^* parameters.

3.4 Cosmic variance and photometric redshift uncertainties

The data set used for our measurement of the LF is the combination of seven catalogues, each one related to a different region of the sky. This allows to keep in principle the effects of cosmic variance to low levels.

In this work, we included a more refined estimate of cosmic variance following the recipe by Moster et al. (2010). A halo distribution model is used to relate the stellar mass to the dark matter halo as a function of redshift; the galaxy bias is then estimated via dissipation-less N-body simulations. The cosmic variance is first computed on dark matter haloes, and then converted to galaxy cosmic variance by applying the galaxy bias. This estimate was cross-checked with the different evaluation of cosmic variance by Driver & Robotham (2010). Their work is based on direct computation of the cosmic variance using M^* galaxies from the SDSS catalogue. The expression found is then generalized to any redshift bin amplitude and mean value and to any geometry of the survey. We find that the two estimates, in the case of M^* galaxies, are consistent within 70% in the lowest redshift bin, but differ up to a factor of 2.5 in the higher redshift ranges. As discussed in Driver & Robotham (2010), this discrepancy can be explained as the change in M^* stellar mass value with redshift.

The computation of the luminosity as a function of mass (or, more frequently, the computation of mass from the luminosity), necessary to obtain the values for cosmic variance is generally a non trivial task, involving the generation of synthetic SEDs based on different initial mass functions, which are then fitted on a per-galaxy basis. For our purposes of cosmic variance estimate in the final LF, we performed the conversion between galaxy baryonic mass M and luminosity L_{JAB} and L_{HAB} a-posteriori on the LF, under the work hypothesis that the mass-to-light ratio can be considered constant over all the involved luminosity range and equal to its average value. We adopted the mean value $\langle M/L \rangle = 1.0^{+0.32}_{-0.27} M_{\odot}/L_{\odot}$ from Cole et al. (2001) for both the J and H bands.

Figure 3 shows as a contour plot the values of the cosmic variance for our data as a function of redshift and galaxy mass, as computed using the Moster et al. cookbook. The values of cosmic

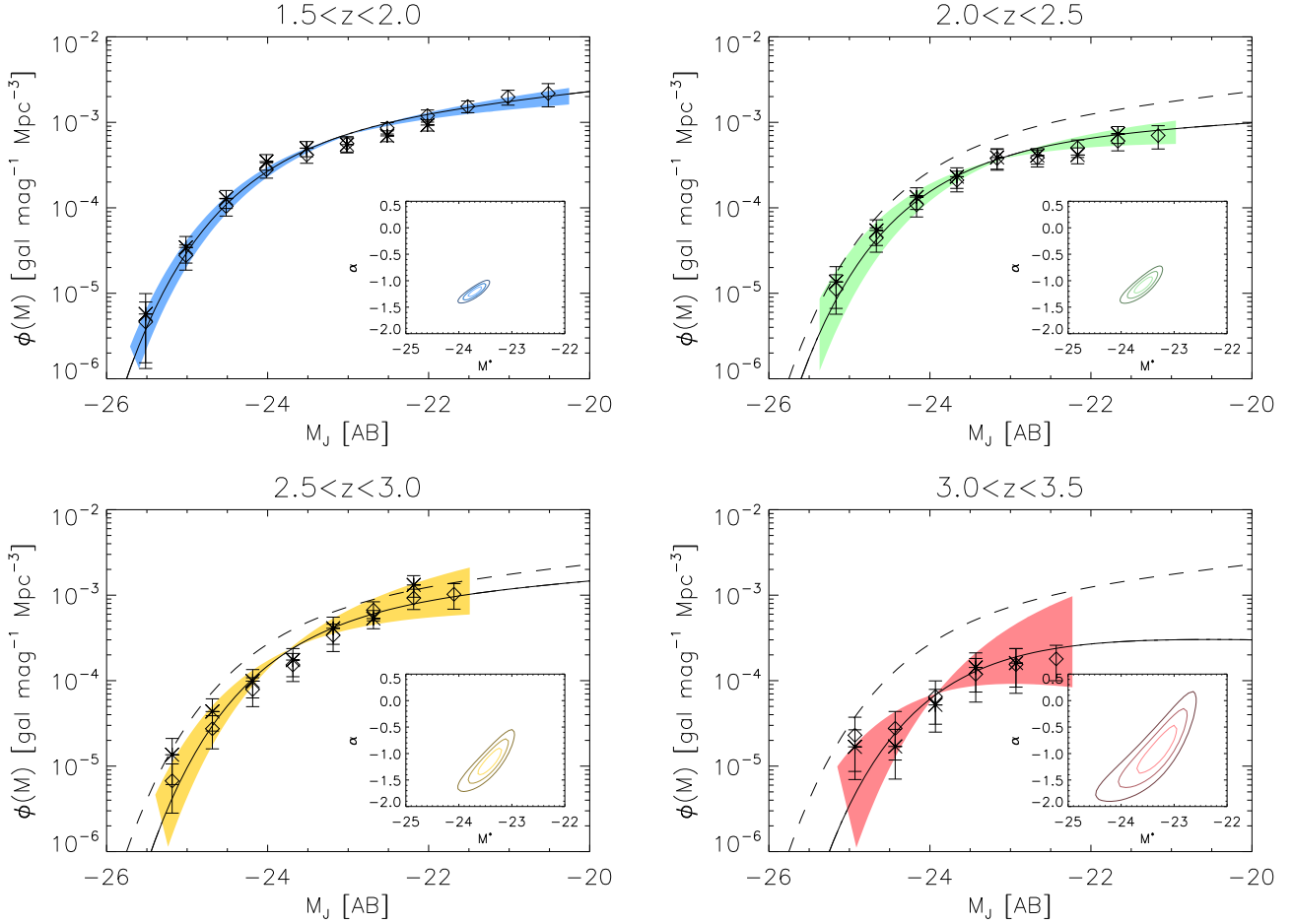


Figure 4. Luminosity function for the rest-frame J band, in the four redshift bins. Asterisks represent the $1/V_{max}$ measurement, diamonds are from the SWML. The Schechter function obtained via the maximum likelihood is shown as the solid black line. The coloured area in each plot indicates the 1σ (68% confidence level) from the parametric maximum likelihood. The inset shows the 1, 2 and 3 σ contours (corresponding to 68%, 95% and 98% confidence region) for the joint α - M^* parameters from the ML analysis. The dashed line marks our $1.5 < z < 2.0$ LF.

variance range from 0.07 to 0.19 in the lowest redshift bin, from 0.09 to 0.24 in the $2.0 < z < 2.5$ bin, from 0.10 to 0.32 in the $2.5 < z < 3.0$ bin and from 0.12 to 0.42 in the $3.0 < z < 3.5$ redshift bin. The recovered uncertainties have been added in quadrature to the standard errors computed in the $1/V_{max}$ and SWML methods, while the cosmic variance corresponding to M^* has been added in quadrature to the error on ϕ^* .

The effects of photometric redshift errors have been studied via Monte Carlo simulations. Five hundred realizations of the LF in each redshift bin were computed. The redshift of each source in the original catalogue was randomly modified according to the gaussian standard deviation recovered from figure 1; the absolute magnitude of each object was then modified accordingly. The distribution of parameters of the recovered LF did not show any systematic effect and the spread of the parameters was compatible with the photometric redshift errors, consistent with the Monte Carlo simulations performed in Marchesini et al. (2007).

4 J - AND H -BAND LUMINOSITY FUNCTIONS

Both rest-frame J - and H -band LFs were estimated in the redshift intervals $1.5 < z < 2.0$, $2.0 < z < 2.5$, $2.5 < z < 3.0$, and $3.0 < z < 3.5$ with the three methods described in Sec. 3. In Table 3 and Table 4 we present our measurements obtained with the SWML and $1/V_{max}$ method, while the derived Schechter parameters in each filter and redshift range are summarized in Table 1 and Table 2.

z range	α	M^*	$\phi^* (10^{-4} \text{ Mag}^{-1} \text{ Mpc}^{-3})$
1.5-2.0	$-1.24^{+0.03}_{-0.03}$	$-23.72^{+0.09}_{-0.06}$	$11.31^{+0.28}_{-0.10}$
2.0-2.5	$-1.12^{+0.11}_{-0.13}$	$-23.60^{+0.14}_{-0.17}$	$7.45^{+0.53}_{-0.38}$
2.5-3.0	$-1.17^{+0.18}_{-0.22}$	$-23.42^{+0.35}_{-0.23}$	$9.73^{+5.37}_{-2.33}$
3.0-3.5	$-0.92^{+0.42}_{-0.48}$	$-23.28^{+0.33}_{-0.39}$	$4.36^{+8.61}_{-1.93}$

Table 1. Schechter parameters for the J LF from the maximum likelihood analysis with one σ errors, including uncertainties from cosmic variance.

z range	α	M^*	$\phi^* (10^{-4} \text{ Mag}^{-1} \text{ Mpc}^{-3})$
1.5-2.0	$-1.30^{+0.04}_{-0.03}$	$-24.03^{+0.06}_{-0.05}$	$8.79^{+0.50}_{-0.20}$
2.0-2.5	$-1.23^{+0.12}_{-0.07}$	$-23.94^{+0.13}_{-0.12}$	$4.35^{+0.68}_{-0.45}$
2.5-3.0	$-1.11^{+0.19}_{-0.18}$	$-23.74^{+0.21}_{-0.23}$	$6.32^{+4.52}_{-1.36}$
3.0-3.5	$-1.30^{+0.40}_{-0.49}$	$-23.89^{+0.36}_{-0.42}$	$2.03^{+8.50}_{-2.04}$

Table 2. Schechter parameters for the H LF from the maximum likelihood analysis with one σ errors, including uncertainties from cosmic variance.

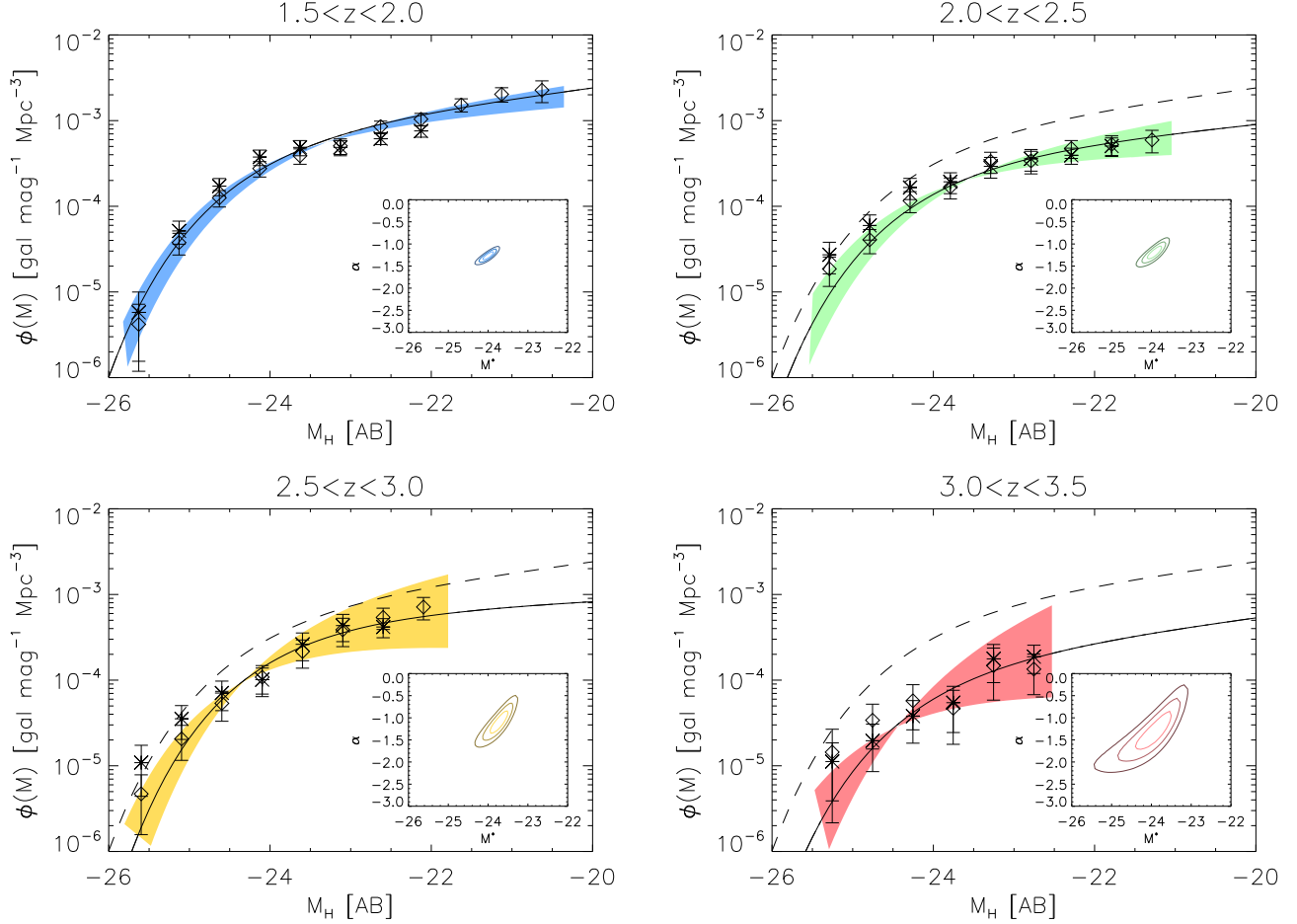


Figure 5. Luminosity function in the H rest frame filter. Plot conventions are the same as for Figure 4.

Figure 4 shows the LF for the rest-frame J filter in the four redshift bins. The number of objects used to construct the LF in each redshift bin are respectively 996, 419, 298 and 103. The three methods return consistent measurements of the LFs.

In Figure 5 we show our measurement of the LF obtained in the H filter, for the same four redshift bins as for the J -band LF. The number of objects used to compute the LF is 996, 419, 298 and 103 respectively for the $1.5 < z < 2.0$, $2.0 < z < 2.5$, $2.5 < z < 3.0$ and $3.0 < z < 3.5$ intervals. To date, this is the first measurement of the rest-frame H -band LF in the interval $z \in [1.5, 3.5]$.

4.1 Comparison with previous works

The measurements by Pozzetti et al. (2003) and Saracco et al. (2006) are the only previously measured rest-frame J -band LFs computed in redshift ranges comparable with ours.

In Pozzetti et al. (2003) the LF is computed for the rest-frame J and rest-frame K bands, using both spectroscopic and photometric data from the K20 survey (Cimatti et al. 2002). Out of the three redshift ranges used to measure the LF ($z \in [0.2, 0.65]$, $[0.75, 1.3]$, $[1.3, 1.9]$), the highest interval is the only one which we can compare to. Their rest-frame J -band LF is shown by the magenta triangles in the left panel of Fig. 6. Our data allow us to compute the LF down to $M_J = -20$, around two magnitudes fainter than their limit; in addition, the area covered by our sam-

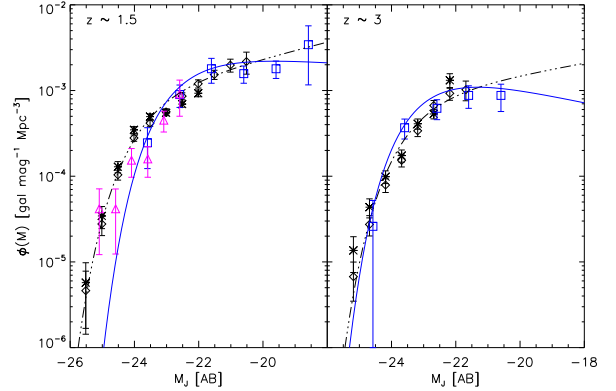


Figure 6. Comparison of Pozzetti et al. (2003) (magenta triangles - left panel) and Saracco et al. (2006) LFs (blue squares and blue solid line) with our measurements (black symbols: asterisks for $1/V_{\max}$, diamonds for the SWML, dash-dotted line for the Schechter parameterization). The left panel refers to $z \approx 1.5$ LF, while the right panel to the $z \approx 3$ LF.

ple is approximately 10 times larger than the area covered by the K20 survey, allowing us to estimate the bright end of the LF more robustly and to a 0.5 mag brighter limit. In the overlapping abso-

z range	M_J [AB]	$SWML[h_{70}^3 mag^{-1} Mpc^{-3}]$	$1/V_{max}[h_{70}^3 mag^{-1} Mpc^{-3}]$
$1.5 < z < 2.0$			
-25.51	$4.78 (\pm 3.30) \pm 3.42 \times 10^{-6}$	$5.65 (\pm 3.99) \pm 4.13 \times 10^{-6}$	
-25.01	$2.87 (\pm 0.77) \pm 0.94 \times 10^{-5}$	$3.39 (\pm 0.98) \pm 1.16 \times 10^{-5}$	
-24.51	$1.08 (\pm 0.14) \pm 0.25 \times 10^{-4}$	$1.27 (\pm 0.19) \pm 0.30 \times 10^{-4}$	
-24.01	$2.90 (\pm 0.25) \pm 0.59 \times 10^{-4}$	$3.42 (\pm 0.31) \pm 0.71 \times 10^{-4}$	
-23.51	$4.44 (\pm 0.35) \pm 0.90 \times 10^{-4}$	$5.03 (\pm 0.38) \pm 1.01 \times 10^{-4}$	
-23.01	$5.90 (\pm 0.49) \pm 1.20 \times 10^{-4}$	$5.82 (\pm 0.43) \pm 1.17 \times 10^{-4}$	
-22.51	$9.09 (\pm 0.84) \pm 1.38 \times 10^{-4}$	$7.80 (\pm 0.62) \pm 1.13 \times 10^{-4}$	
-22.01	$1.26 (\pm 0.14) \pm 0.20 \times 10^{-3}$	$9.39 (\pm 0.84) \pm 1.41 \times 10^{-4}$	
-21.51	$1.61 (\pm 0.20) \pm 0.25 \times 10^{-3}$	-	
-21.01	$2.08 (\pm 0.36) \pm 0.41 \times 10^{-3}$	-	
-20.51	$2.29 (\pm 0.66) \pm 0.69 \times 10^{-3}$	-	
$2.0 < z < 2.5$			
-25.17	$1.36 (\pm 0.52) \pm 0.61 \times 10^{-5}$	$1.61 (\pm 0.66) \pm 0.77 \times 10^{-5}$	
-24.67	$4.52 (\pm 0.91) \pm 1.44 \times 10^{-5}$	$5.36 (\pm 1.20) \pm 1.78 \times 10^{-5}$	
-24.17	$1.15 (\pm 0.15) \pm 0.32 \times 10^{-4}$	$1.38 (\pm 0.19) \pm 0.39 \times 10^{-4}$	
-23.67	$2.24 (\pm 0.25) \pm 0.61 \times 10^{-4}$	$2.65 (\pm 0.29) \pm 0.71 \times 10^{-4}$	
-23.17	$4.08 (\pm 0.47) \pm 1.11 \times 10^{-4}$	$4.48 (\pm 0.48) \pm 1.20 \times 10^{-4}$	
-22.67	$4.22 (\pm 0.64) \pm 0.92 \times 10^{-4}$	$4.36 (\pm 0.58) \pm 0.89 \times 10^{-4}$	
-22.17	$5.52 (\pm 0.93) \pm 1.27 \times 10^{-4}$	$4.24 (\pm 0.59) \pm 0.89 \times 10^{-4}$	
-21.67	$6.51 (\pm 1.28) \pm 1.50 \times 10^{-4}$	$7.48 (\pm 1.41) \pm 1.67 \times 10^{-4}$	
-21.17	$7.58 (\pm 2.12) \pm 2.31 \times 10^{-4}$	-	
$2.5 < z < 3.0$			
-25.19	$8.41 (\pm 3.73) \pm 4.62 \times 10^{-6}$	$1.61 (\pm 0.66) \pm 0.84 \times 10^{-5}$	
-24.69	$2.82 (\pm 0.76) \pm 1.19 \times 10^{-5}$	$4.43 (\pm 1.11) \pm 1.81 \times 10^{-5}$	
-24.19	$8.45 (\pm 1.54) \pm 3.14 \times 10^{-5}$	$1.21 (\pm 0.21) \pm 0.44 \times 10^{-4}$	
-23.69	$1.68 (\pm 0.27) \pm 0.60 \times 10^{-4}$	$2.19 (\pm 0.36) \pm 0.79 \times 10^{-4}$	
-23.19	$3.78 (\pm 0.53) \pm 1.33 \times 10^{-4}$	$4.35 (\pm 0.58) \pm 1.52 \times 10^{-4}$	
-22.69	$7.48 (\pm 1.07) \pm 1.88 \times 10^{-4}$	$5.80 (\pm 0.73) \pm 1.40 \times 10^{-4}$	
-22.19	$1.03 (\pm 0.17) \pm 0.27 \times 10^{-3}$	-	
-21.69	$1.14 (\pm 0.29) \pm 0.38 \times 10^{-3}$	-	
$3.0 < z < 3.5$			
-24.93	$2.64 (\pm 1.25) \pm 1.67 \times 10^{-5}$	$1.83 (\pm 0.75) \pm 1.07 \times 10^{-5}$	
-24.43	$3.81 (\pm 1.42) \pm 2.13 \times 10^{-5}$	$2.51 (\pm 1.13) \pm 1.54 \times 10^{-5}$	
-23.93	$9.80 (\pm 1.67) \pm 4.43 \times 10^{-5}$	$7.45 (\pm 2.23) \pm 3.83 \times 10^{-5}$	
-23.43	$1.68 (\pm 0.14) \pm 0.72 \times 10^{-4}$	$1.54 (\pm 0.38) \pm 0.75 \times 10^{-4}$	
-22.93	$2.19 (\pm 0.25) \pm 0.95 \times 10^{-4}$	$2.82 (\pm 1.35) \pm 1.79 \times 10^{-4}$	
-22.43	$2.55 (\pm 0.47) \pm 0.83 \times 10^{-4}$	-	

Table 3. Luminosity function values obtained with the SWML and $1/V_{max}$ methods in the four redshift bins for the J filter. The first error value refers to the error estimated via the information matrix for the SWML method and to the Poisson error for the $1/V_{max}$ method, while the second term is the cumulative error taking into account also cosmic variance uncertainties.

lute magnitude range, the two measured LFs are in good agreement within the $1 - \sigma$ errors.

Saracco et al. (2006) estimated the J -band LF in three redshift ranges, namely $z < 0.8$, $0.8 < z < 1.9$ and $1.9 < z < 4.0$, using 101, 100, and 84 galaxies, respectively, collected from the HDF-S data and complemented by VLT-ISAAC J,H and K imaging. The LFs from Saracco et al. (2006) are compared to our measurements in Figure 6. At $z \approx 1.5$, the absolute magnitude ranges of the two determinations are quite different. Their lack of points at the bright end, presumably due to the very small field of the HDF-S compared to ours, is compensated by a deeper limit at the faint end. Their Schechter representation of the LF is flatter ($\alpha = -0.94$) than our measurement of the LF at $1.5 < z < 2.0$, and it presents a dimmer characteristic magnitude (by ~ 1 mag). However, when directly comparing the $1/V_{max}$ estimate from Saracco et al. (2006) with our non parametric $1.5 < z < 2.0$ LF, we find good agreement (see Figure 6, left panel) with measurements lying within the 1σ error bars. Despite these differences, our Schechter parameterization is substantially compatible also with their points. We would like to note that our composite catalogue provides an improved sampling of the bright end, resulting in overall better constrained Schechter parameters, due to the strong correlation among these parameters. In the highest redshift bin, the differences in the Schechter parameters are still present, with the faint-end slope α being the parameter showing the largest difference. As for the lower-redshift bin, when comparing our non parametric estimate with their points, we find a good agreement (see the right panel in Figure 6).

z range	M_H [AB]	$SWML[h_{70}^3 mag^{-1} Mpc^{-3}]$	$1/V_{max}[h_{70}^3 mag^{-1} Mpc^{-3}]$
$1.5 < z < 2.0$			
-25.63	$4.12 (\pm 2.85 \pm 2.95 \times 10^{-6}$	$5.69 (\pm 4.02) \pm 4.16 \times 10^{-6}$	
-25.13	$3.71 (\pm 0.79) \pm 1.05 \times 10^{-5}$	$5.08 (\pm 1.20) \pm 1.53 \times 10^{-5}$	
-24.63	$1.24 (\pm 0.14) \pm 0.27 \times 10^{-4}$	$1.69 (\pm 0.22) \pm 0.38 \times 10^{-4}$	
-24.13	$2.74 (\pm 0.23) \pm 0.56 \times 10^{-4}$	$3.73 (\pm 0.33) \pm 0.77 \times 10^{-4}$	
-23.63	$3.92 (\pm 0.32) \pm 0.80 \times 10^{-4}$	$4.91 (\pm 0.37) \pm 0.99 \times 10^{-4}$	
-23.13	$5.04 (\pm 0.44) \pm 1.04 \times 10^{-4}$	$4.86 (\pm 0.38) \pm 0.98 \times 10^{-4}$	
-22.63	$8.61 (\pm 0.81) \pm 1.32 \times 10^{-4}$	$6.19 (\pm 0.50) \pm 0.90 \times 10^{-4}$	
-22.13	$1.04 (\pm 0.12) \pm 0.17 \times 10^{-3}$	$7.49 (\pm 0.73) \pm 1.16 \times 10^{-4}$	
-21.63	$1.53 (\pm 0.19) \pm 0.27 \times 10^{-3}$	-	
-21.13	$2.03 (\pm 0.34) \pm 0.39 \times 10^{-3}$	-	
-20.63	$2.26 (\pm 0.61) \pm 0.64 \times 10^{-3}$	-	
$2.0 < z < 2.5$			
-25.29	$2.04 (\pm 0.55) \pm 0.74 \times 10^{-5}$	$2.95 (\pm 0.89) \pm 1.15 \times 10^{-5}$	
-24.79	$4.06 (\pm 0.80) \pm 1.28 \times 10^{-5}$	$5.89 (\pm 1.26) \pm 1.92 \times 10^{-5}$	
-24.29	$1.23 (\pm 0.15) \pm 0.34 \times 10^{-4}$	$1.74 (\pm 0.22) \pm 0.48 \times 10^{-4}$	
-23.79	$1.76 (\pm 0.21) \pm 0.48 \times 10^{-4}$	$2.02 (\pm 0.23) \pm 0.55 \times 10^{-4}$	
-23.29	$3.46 (\pm 0.44) \pm 0.96 \times 10^{-4}$	$2.97 (\pm 0.34) \pm 0.81 \times 10^{-4}$	
-22.79	$3.62 (\pm 0.57) \pm 1.06 \times 10^{-4}$	$3.75 (\pm 0.51) \pm 1.05 \times 10^{-4}$	
-22.29	$5.04 (\pm 0.88) \pm 1.18 \times 10^{-4}$	$4.36 (\pm 0.71) \pm 0.99 \times 10^{-4}$	
-21.79	$5.56 (\pm 1.14) \pm 1.44 \times 10^{-4}$	$5.05 (\pm 0.94) \pm 1.23 \times 10^{-4}$	
-21.29	$6.27 (\pm 1.69) \pm 2.12 \times 10^{-4}$	-	
$2.5 < z < 3.0$			
-25.60	$5.69 (\pm 2.93) \pm 3.46 \times 10^{-6}$	$1.34 (\pm 0.60) \pm 0.74 \times 10^{-5}$	
-25.10	$1.91 (\pm 0.58) \pm 0.84 \times 10^{-5}$	$3.49 (\pm 0.97) \pm 1.49 \times 10^{-5}$	
-24.60	$5.21 (\pm 1.06) \pm 1.99 \times 10^{-5}$	$6.98 (\pm 1.37) \pm 2.64 \times 10^{-5}$	
-24.10	$1.05 (\pm 0.18) \pm 0.39 \times 10^{-4}$	$9.98 (\pm 1.72) \pm 3.65 \times 10^{-5}$	
-23.60	$2.20 (\pm 0.35) \pm 0.79 \times 10^{-4}$	$2.67 (\pm 0.39) \pm 0.95 \times 10^{-4}$	
-23.10	$3.93 (\pm 0.65) \pm 1.43 \times 10^{-4}$	$4.40 (\pm 0.59) \pm 1.54 \times 10^{-4}$	
-22.60	$5.56 (\pm 1.03) \pm 1.54 \times 10^{-4}$	$4.25 (\pm 0.60) \pm 1.06 \times 10^{-4}$	
-22.10	$7.23 (\pm 1.51) \pm 2.12 \times 10^{-4}$	-	
$3.0 < z < 3.5$			
-25.25	$1.40 (\pm 1.02) \pm 1.17 \times 10^{-5}$	$1.10 (\pm 0.55) \pm 0.72 \times 10^{-5}$	
-24.75	$3.32 (\pm 1.13) \pm 1.79 \times 10^{-5}$	$1.93 (\pm 0.73) \pm 1.09 \times 10^{-5}$	
-24.25	$6.10 (\pm 1.98) \pm 3.23 \times 10^{-5}$	$4.11 (\pm 1.19) \pm 2.10 \times 10^{-5}$	
-23.75	$4.69 (\pm 2.10) \pm 2.87 \times 10^{-5}$	$5.38 (\pm 1.94) \pm 2.97 \times 10^{-5}$	
-23.25	$1.47 (\pm 0.62) \pm 0.87 \times 10^{-4}$	$1.77 (\pm 0.39) \pm 0.84 \times 10^{-4}$	
-22.75	$1.35 (\pm 0.54) \pm 0.65 \times 10^{-4}$	$1.88 (\pm 0.45) \pm 0.68 \times 10^{-4}$	

Table 4. Luminosity function values obtained with the SWML and $1/V_{max}$ methods in the four redshift bins for the H filter. The first error value refers to the error estimated via the information matrix for the SWML method and to the Poisson error for the $1/V_{max}$ method, while the second term is the cumulative error taking into account also cosmic variance uncertainties.

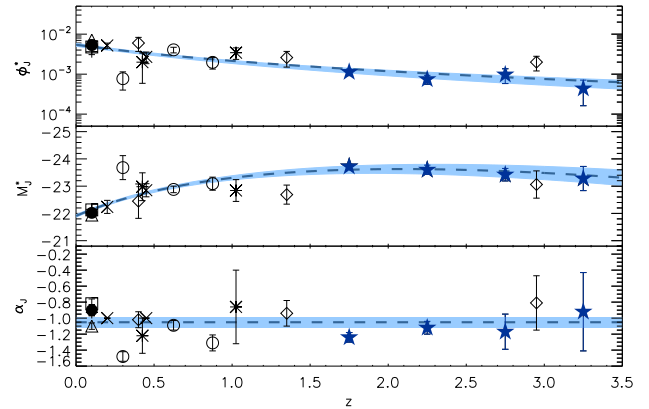


Figure 7. Evolution of the Schechter parameters of the J LF as a function of redshift. Estimates from this work are shown as filled blue stars. Measurements from the literature are also plotted (vertical crosses: Cole et al. 2001; asterisks: Pozzetti et al. 2003; crosses: Feulner et al. 2003; open squares: Eke et al. 2005; open circles: Dahlen et al. 2005; open diamonds: Saracco et al. 2006; open triangles: Jones et al. 2006; filled circle: Hill et al. 2010). Top panel shows the data for ϕ^* . The dashed line represents Eq. 10 (see text for details); the middle panel presents the measurements for M^* , with the dashed line representing Eq. 11; in the lower panel the faint end slopes α together with the average value (dashed line) are shown. The filled regions correspond to 95% confidence level intervals for the resulting fitting curves.

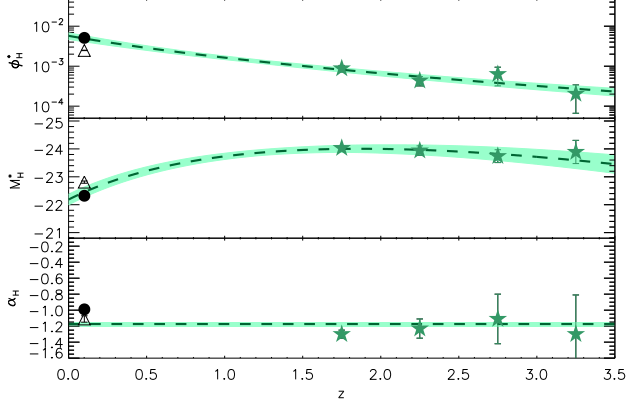


Figure 8. Evolution of the Schechter ϕ^* , M^* and α parameters from the H LF as a function of redshift. See caption to Figure 7 for details.

4.2 Discussion

In Figure 7 we compare the Schechter parameters for the rest-frame J band obtained in this work with those available in the literature as a function of redshift.

The upper panel shows the evolution of ϕ^* as a function of redshift, showing ϕ^* monotonically decreasing with increasing z . By $z \simeq 2$, ϕ^* has decreased by approximately an order of magnitude compared to the local values. The following parameterization was adopted to model the observed evolution of ϕ^* with z :

$$\phi^*(z) = \theta \exp \left[\gamma / (1 + z)^\beta \right] \quad (10)$$

where θ , γ , and β are the free parameters. The best-fit values obtained for the parameters of the rest-frame J band are $\theta_J = 2.6 \pm 0.9 \times 10^{-6} \text{ mag}^{-1} \text{ Mpc}^{-3}$, $\gamma_J = 7.7 \pm 0.3$, $\beta_J = 0.22$. The β parameter was estimated together with the other two in the first instance of the best fitting procedure, and kept fix in a second iteration. The quoted errors refer to the second iteration. Equation 10 is plotted as a dashed line in the upper panel of Figure 7.

In the middle panel of Fig. 7 we present the evolution of M^* as a function of redshift. The data show a brightening of M^* from the local universe to $z \simeq 2$, followed by a slow dimming. In analogy to the LF shape by Schechter (1976), it is then possible to introduce the following ad-hoc representation for $M^*(z)$:

$$M^*(z) = \mu [(1 + z)/(1 + z^*)]^\eta \exp [-(1 + z)/(1 + z^*)] \quad (11)$$

with μ , z^* , and η free parameters to be determined. By performing a least-square fit to the available data we obtain the following values: $\mu_J = -37.6 \pm 1.7 \text{ mag}$, $z_J^* = 17.5 \pm 4.6$, $\eta_J = 0.16 \pm 0.02$. The resulting curve is plotted as a dashed line in the middle panel of Figure 7.

The lower panel illustrates the behavior of α as a function of redshift. The error bars are here generally large and do not allow to properly evaluate the presence of evolution as a function of z . Therefore we limit ourselves to compute an average value, resulting in $\bar{\alpha} = -1.05 \pm 0.03$.

Figure 8 shows the plots of the Schechter parameters as a function of redshift corresponding to the rest-frame H band. For this band, there are only two determinations of the LF from the literature, making it more challenging to determine the evolution with redshift. Despite this, we applied the same analysis done for the rest-frame J band, obtaining $\theta_H = 2.0 \pm 1.3 \times 10^{-6} \text{ mag}^{-1} \text{ Mpc}^{-3}$, $\gamma_H = 7.8 \pm 0.5$, $\beta_H = 0.30$ for the parameters of Eq.

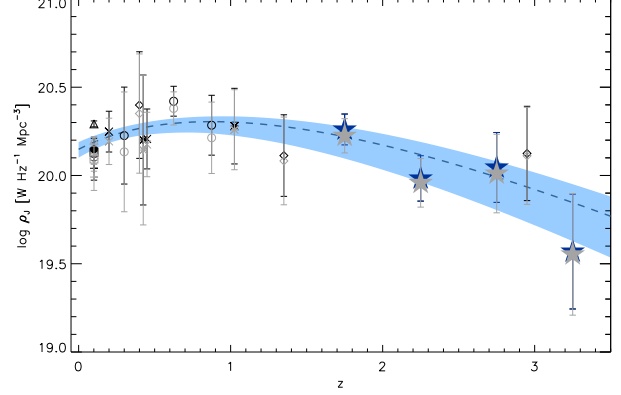


Figure 9. Luminosity density ρ_J as computed from our Schechter parameters (filled blue stars) and compared with the available data in the redshift range $[0,3.0]$. Grayed symbols indicate the luminosity density computed assuming an absolute magnitude limit of $M_J = -20.0$. The dashed line represents the LD obtained directly from Eq. 12 in terms of Eq. 10 and 11, with 95% confidence level indicated by the filled region. Plotting symbols same as for Fig. 7.

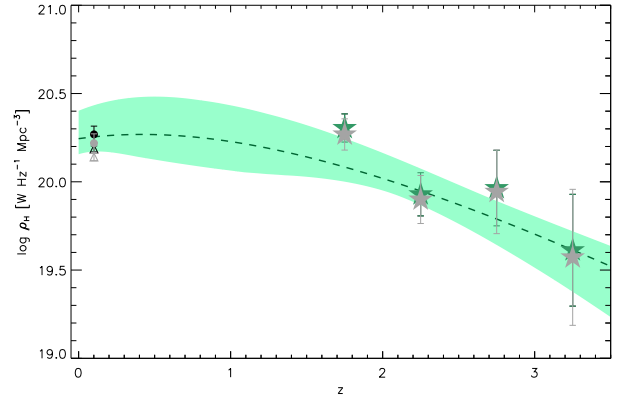


Figure 10. Luminosity density ρ_H as computed from our Schechter parameters (filled black stars) and compared with the available data. See caption to Fig. 9 for details.

10; $\mu_H = -40.0 \pm 9.3$, $z_H^* = 13.9 \pm 6.3$, $\eta_H = 0.19 \pm 0.06$ for Eq. 11 and $\bar{\alpha} = -1.15 \pm 0.02$. The resulting best-fits are shown as dashed curves in Figure 8.

4.3 Luminosity densities

Here we present our measurements of the luminosity density (LD). Given the coupling between the Schechter parameters α and M^* , the luminosity density is a robust tool to characterize the evolution of the LF with cosmic time. The LD was obtained in the standard way, i.e. as:

$$\rho_J = \int_0^{+\infty} L \Phi(L) dL = \Gamma(2 + \alpha) L^* \phi^* \quad (12)$$

where the last equality holds when assuming a Schechter parametrization for the $\Phi(L)$. This means that we are assuming that the Schechter distribution is a good representation of the underlying luminosity function. Figure 9 shows the evolution of the

Filter	z range	$\log \rho$	$\log \rho^*$	$\log \bar{\rho}$
<i>J</i>	1.5-2.0	20.26 ± 0.08	20.22 ± 0.09	20.22 ± 0.09
	2.0-2.5	19.98 ± 0.12	19.96 ± 0.13	19.93 ± 0.13
	2.5-3.0	20.05 ± 0.18	20.01 ± 0.20	19.93 ± 0.24
	3.0-3.5	19.57 ± 0.30	19.55 ± 0.32	19.45 ± 0.39
<i>H</i>	1.5-2.0	20.30 ± 0.08	20.27 ± 0.09	20.27 ± 0.09
	2.0-2.5	19.93 ± 0.12	19.90 ± 0.14	19.87 ± 0.14
	2.5-3.0	19.96 ± 0.21	19.94 ± 0.24	19.85 ± 0.28
	3.0-3.5	19.61 ± 0.32	19.57 ± 0.38	19.39 ± 0.52

Table 5. Luminosity density in logarithmic scale and expressed in units of $\log[\text{W Hz}^{-1} \text{Mpc}^{-3}]$, in the rest-frame *J* and *H* bands. Quoted errors include the effects of cosmic variance, which is the dominant source of random uncertainties. In the third column we report the luminosity density computed using Eq. 12 and corresponding to the black stars in Figures 9 and 10; the values of the luminosity density in the fourth column ($\log \rho^*$) reflect the upper limit in absolute magnitude corresponding to $M_{lim} = -20$, which we imposed in order to limit the effect of the uncertainties in the determination of α (grey stars in the same figures). The values in the last column ($\log \bar{\rho}$) list the luminosity densities computed using the corresponding absolute magnitude limits at each redshift bin and for each band, i.e., $M_{J,lim} = -20, -21, -21.5, -22$, and $M_{H,lim} = -20, -21, -22, -22.5$ for the redshift intervals centered at $z = 1.75, 2.25, 2.75, 3.25$, respectively.

luminosity density in the *J* filter, while Figure 10 displays the corresponding plot for the rest-frame *H* band. Values of the luminosity density at each redshift and for each filter are presented in Table 5.

In order to be less sensitive to the derived faint end slope of the LF, we also computed the luminosity density assuming two different limiting absolute magnitudes. First, the luminosity density $\bar{\rho}$ was derived using the absolute magnitude limits of our survey in each redshift bin, i.e., $M_{J,lim} = -20, -21, -21.5, -22$, and $M_{H,lim} = -20, -21, -22, -22.5$, for the redshift intervals centered at $z = 1.75, 2.25, 2.75, 3.25$, respectively. Second, the luminosity density ρ^* was derived assuming a limiting absolute magnitude equal to the brightest limit over the entire targeted redshift range, i.e. $M_{lim} = -20.0$. The values of ρ^* are also plotted in Figures 9 and 10 as grey symbols.

The overall plot of the *J*-band luminosity density shows a constant value for $z \lesssim 0.8 - 1.0$. At $z \approx 0.8 - 1.0$, the luminosity density starts to decrease down to $z \approx 3.5$, where ρ_J is 16% of the $z = 0$ value. This can be better visualized by comparing this plot with the top and middle panels of Figure 7. Here we see in fact that for $z \lesssim 1$ the decrease in number of galaxies is balanced by a brightening of the characteristic magnitude. At $z \gtrsim 1$, both quantities decrease, with the resulting decrease of the luminosity density.

Using the expression of Eq. 10 and Eq. 11 in Eq. 12, it is possible to obtain a functional representation of the luminosity density. The dashed line in Figure 9 represents the luminosity density for the rest-frame *J* band obtained with this method and adopting the best-fit values of the parameters previously recovered. The agreement with the points is good over the entire redshift range. We would like to stress that no best fit has been done using the data of the luminosity density.

Similarly to the case of the LF, the luminosity density in the *H* filter has been poorly studied, so that it is more difficult to derive its evolution. Our data however indicate a decline with redshift of the LD, similar in shape to the one found in the *J* band, with a faster evolution from $z = 3.5$ to $z = 1.5$, followed by a much slower evolution, decreasing by a factor of ~ 7 from $z = 0$ to $z = 3.5$.

An exercise similar to what done for the *J*-band luminosity density, introducing our parameterizations, is shown as a dashed line in Figure 10. The agreement is quite good over the whole redshift range, although more measurements are necessary at intermediate redshifts ($z < 1.5$).

4.4 Comparison with rest-frame *K*-band LF and LD

In Fig. 11 we present the evolution of the Schechter parameters ϕ^* (top panel) and M^* (bottom panel) for the rest-frame *K* band, collected from the literature (coloured points - see legend for details) and overplotted to the corresponding parameterization of the rest-frame *J* band (taken from Fig. 7; black line). The previously measured rest-frame *K*-band LFs are taken from Mobasher, Sharples, & Ellis (1993); Glazebrook et al. (1995); Cowie et al. (1996); Gardner et al. (1997); Szokoly et al. (1998); Loveday (2000); Kochanek et al. (2001); Cole et al. (2001); Bolzonella, Pelló, & Maccagni (2002); Feulner et al. (2003); Huang et al. (2003); Pozzetti et al. (2003); Kashikawa et al. (2003); Saracco et al. (2006); Caputi et al. (2006); Cirasuolo et al. (2007, 2010) - see also Table 5 in Saracco et al. (2006) which we used as reference for the literature works.

Using the rest-frame *K*-band data, we performed the same analysis as done for the rest-frame *J* and *H* bands, modeling the evolution of the Schechter parameters with redshift using Eq. 10 and 11. The best-fit values of the parameters obtained in modeling of the *K*-band points are: $\theta_K = 3.8 \pm 0.1 \times 10^{-3} \text{ mag}^{-1} \text{Mpc}^{-3}$, $\gamma_K = -0.11 \pm 0.02$, $\beta_K = -2.2 \pm 0.1$ for the parameters of Eq. 10; $\mu_K = -29.6 \pm 0.4$, $z_K^* = 113 \pm 46$, $\eta_K = 0.058 \pm 0.007$ for Eq. 11; and $\bar{\alpha}_K = -1.12 \pm 0.16$. The resulting curves are plotted in Fig. 11 as red dot-dashed curves, together with those already discussed for the rest-frame *J* band (black dashed curves).

The rest-frame *K*-band characteristic density, ϕ_K^* , decreases by a factor of ~ 15 from $z \sim 0$ to $z \sim 3.3$, about twice as much than the redshift evolution of the rest-frame *J*-band characteristic density, ϕ_J^* . Specifically, the data in the rest-frame *J* band indicate an evolution with redshift broadly consistent to the rest-frame *K* band out to $z \sim 2.3$, and a milder evolution at $z \gtrsim 2$. Quantitatively, while ϕ_J^* decreases by a factor of ~ 2 from $z \sim 1.5$ to $z \sim 3.3$, ϕ_K^* decreases by a factor of ~ 5 over the same redshift interval, although these differences are significant only at the 2σ level.

Differences between the rest-frame *J* band and the rest-frame *K* band are also found when comparing the evolution with redshift of the characteristic magnitudes M_K^* and M_J^* (bottom panel of Fig. 11). At $z \lesssim 1$, similar evolutions with redshift of M_K^* and M_J^* are found, with the characteristic magnitudes brightening by $\sim 0.8 \text{ mag}$ from $z \sim 0$ to $z \sim 1$. However, for $z \gtrsim 1$, M_K^* is monotonically decreasing, brightening by 0.5 mag in the range $z \in [1.5, 3.3]$, whereas M_J^* shows a small dimming (if any) over the same redshift interval, after reaching its brightest value somewhere in the redshift interval $1.5 < z < 2.5$. We note that, also in the case of M^* , these differences are only marginally significant (within 2σ).

Figure 12 shows the comparison of the evolutions with redshift of the rest-frame *K*- and *J*-band LDs. As the differences in the evolutions with redshift of ϕ^* and M^* between the *J* and *K* bands go in opposite directions, in the computation of the LDs these differences partly cancel out. As shown in Figure 12, the evolution of the rest-frame *K*-band LD with redshift is qualitatively similar to the evolution with redshift of the rest-frame *J*-band LD, decreasing by a factor of almost ~ 2 from $z \sim 0$ to $z \sim 2.5$.

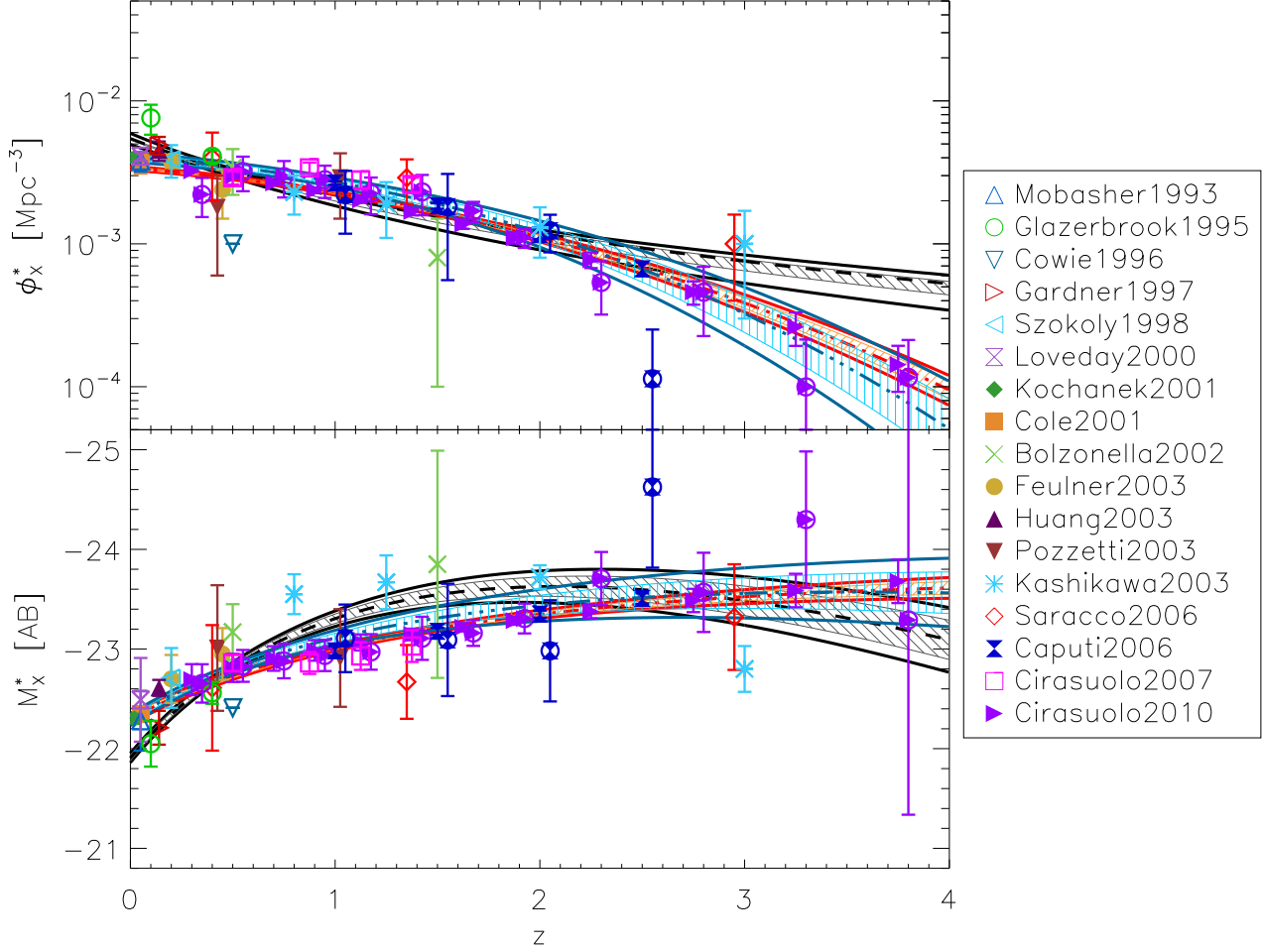


Figure 11. Top panel: comparison between the evolution with redshift of the Schechter parameter ϕ^* in the rest-frame J and K (coloured points - see the legend on the right for details) bands. For the Caputi et al. (2006) and Cirasuolo et al. (2010) LFs, the parameter values recovered from a Schechter fit to the $1/V_{\max}$ LFs are identified by an additional circle and are displaced by an arbitrary amount of 0.05 in redshift to increase readability. The black dashed curve shows the best-fit parameterizations obtained for the rest-frame J band. The red and the blue curves mark the best-fit parameterization for the K band using the original ML from Caputi et al. (2006) and Cirasuolo et al. (2010) and that using the points from the Schechter fit to their $1/V_{\max}$ LFs, respectively. The hatched regions delimit the 68% confidence level for the fit parameters for the rest-frame J band (grey), K band (orange), and K band with Schechter parameters obtained from fitting the $1/V_{\max}$ LFs (cyan), respectively. 95% confidence intervals are also plotted as coloured solid black, red, and blue curves, respectively. Bottom panel: evolution with redshift of the rest-frame J - and K -band characteristic magnitude M^* . Same plotting conventions as top panel apply.

The evolution of the K -band LF (and, consequently, LD) at $z \gtrsim 1$ is dominated by the measurements by Caputi et al. (2006) and Cirasuolo et al. (2010), obtained adopting ad-hoc parameterizations for ϕ_K^* and M_K^* , with $\phi_K^*(z) \propto \exp(-z^{\eta_\phi})$ and $M_K^*(z) \propto z^{\eta_M}$ (see Eq. 2 and 3 in Cirasuolo et al. 2010 for details). In order to verify that the derived redshift evolution in the rest-frame K band does not depend on the adopted parameterizations, we computed the Schechter function parameters by fitting their $1/V_{\max}$ estimates with a Schechter function with M_K^* , ϕ_K^* and α_K as free parameters. The results are indicated in Fig. 11 and Fig. 12 by an additional circle around the corresponding symbol, while our evolutionary-model best fits (Eq. 10 and 11) are shown by the blue curves. The values of the Schechter parameters recovered from the fit to the $1/V_{\max}$ measurements are in broad agreement with those obtained from the ML analysis in combination with the adopted $\phi_K^*(z)$ and $M_K^*(z)$ parameterizations, although with larger error bars. Consequently, the evolution with redshift of ϕ_K^* and M_K^* inferred from

the Schechter parameters obtained from the fit to the $1/V_{\max}$ measurements partly overlap to that obtained using the original ML data of Caputi et al. (2006) and Cirasuolo et al. (2010), although with significantly larger errors.

The final picture is that globally the evolutions of the rest-frame J - and K -band LFs are (marginally) different within a confidence level not exceeding the 95% (i.e. roughly 2σ). The LDs in the two rest-frame bands are consistent up to $z \sim 2.5$. At $z \gtrsim 2.5$, there seems evidence of a faster decrease with redshift of the rest-frame K -band LD compared to the rest-frame J -band LD at 68% confidence level. However, the evolutions of the LDs in the two bands are comparable when considering the 95% confidence level. We note that the measurements of the K -band LDs derived from the Schechter function fits to the $1/V_{\max}$ analysis from Caputi et al. (2006) and Cirasuolo et al. (2010) are consistent with our estimated rest-frame J -band LDs within the errors. More accurate measurements of the LFs at $z \gtrsim 2.5$ in both the J and K

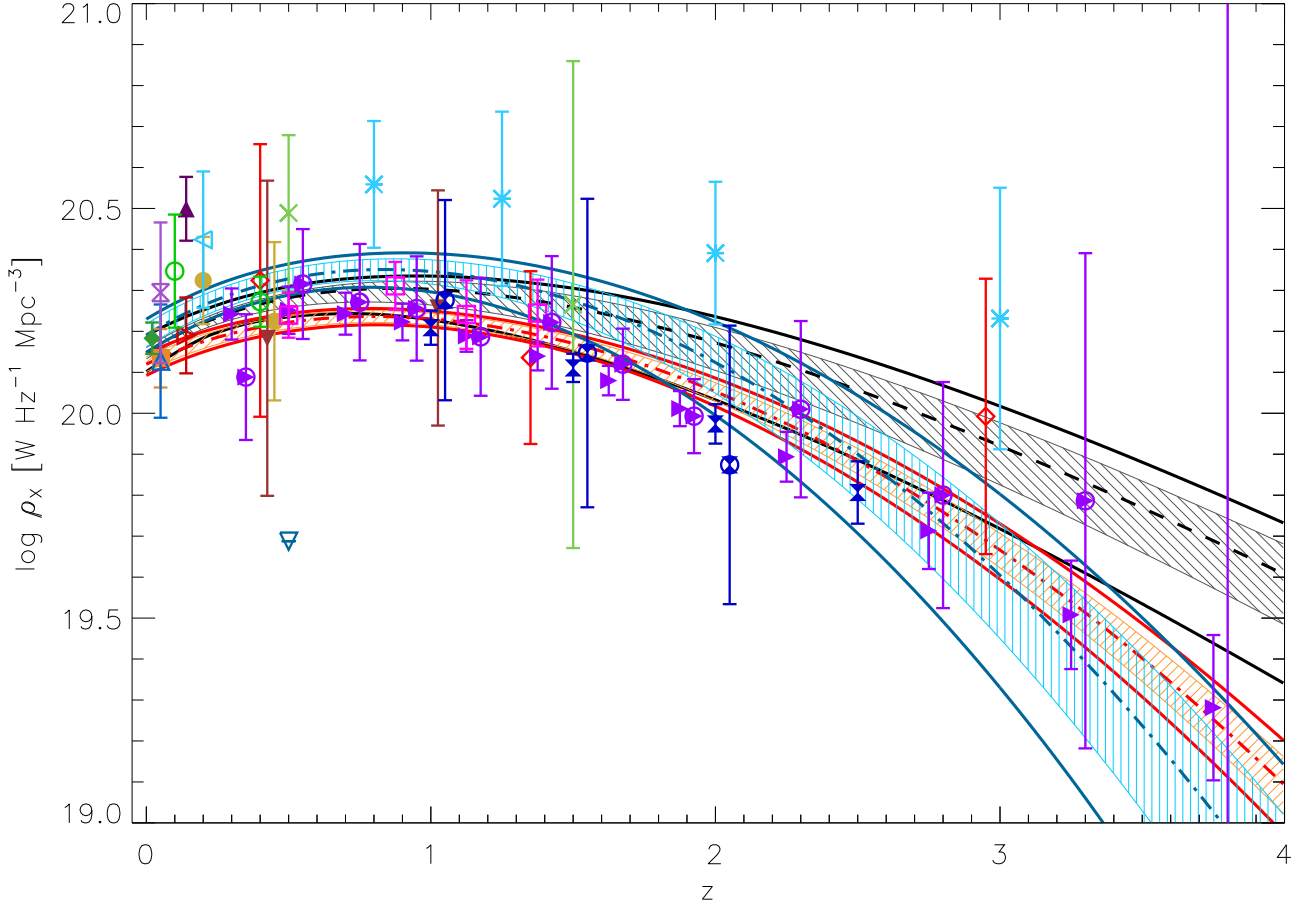


Figure 12. Comparison between the evolution with redshift of the LD in the rest-frame *J* (black curves and gray hatched regions - same plotting conventions as for Fig. 7) and *K* bands (coloured points - same plotting conventions as for Fig. 11). The hatched regions delimit the 68% confidence levels for the fit parameters, while the external coloured solid curves delimit the 95% confidence levels.

bands are required to further investigate possible differences in the redshift evolution of the LDs in the two NIR bands.

Figures 11 and 12 show the presence of significant scatter in the measurements of the rest-frame *K*-band characteristic magnitudes M_K^* and LDs from different works (up to a factor of ~ 2 -3 when comparing the works of Kashikawa et al. 2003 and Cirasuolo et al. 2010). Whereas it is difficult to assess the sources of such scatter and beyond the scopes of this work, we note that potential sources for such a significant scatter are twofold.

First, any direct measurements of the rest-frame *K*-band LF and LD at $z \gtrsim 0.6$ require observations at wavelengths longer than $2.2 \mu\text{m}$, provided by, e.g., Spitzer-IRAC. As Caputi et al. (2006), Cirasuolo et al. (2007), and Cirasuolo et al. (2010) are the only previous works targeting the rest-frame *K* band including IRAC data in their analysis, all the other works do not directly probe the rest-frame *K* band, but instead rely on stellar population synthesis models or empirical templates to extrapolate the rest-frame *K*-band magnitudes of galaxies. Therefore, some of the scatter observed in the measurements of the rest-frame *K*-band LF parameters and LDs at $z \lesssim 2.5$ could be due to differences in the adopted stellar population synthesis models, such as differences in the implementation of the TP-AGB phase (i.e., Bruzual & Charlot 2003; Maraston 2005). Note that observations at wavelengths longer than

provided by IRAC would be needed to directly probe the rest-frame *K* band at $z \gtrsim 2.6$, so all measurements of the rest-frame *K*-band LF and LD at $z \gtrsim 2.6$ rely on stellar models.

Second, emission associated to obscured (e.g., type-II) AGN (e.g., continuum emission from the dusty torus) can be significant in the rest-frame *K* band and at longer wavelengths. At low redshifts ($z < 0.15$), nuclear contamination in the *K* band from (obscured) AGN has been shown to be $\sim 25\%$ on average in radio galaxies, and as high as 40% (on average) in broad-lined radio galaxies (Inskip et al. 2010). AGN contamination are generally much smaller in the rest-frame *J* or *H* bands, with an average contamination of ~ 3 -4% (e.g., Floyd et al. 2008). We note that, while these levels of AGN contamination have been derived for radio-loud AGNs, which represent only $\sim 10\%$ of the overall AGN population, radio-quiet AGNs are expected to be characterized by similar levels of contamination, as a result of the similar orientation-based unification scheme (Antonucci 1993; Hönig et al. 2006). Moreover, evidence for an increasing fraction of AGN as a function of stellar mass at $z > 2$ has been recently found, with an AGN fraction as high as 70% for massive galaxies at $2.0 < z < 2.7$ (Kriek et al. 2007), and potentially even higher AGN fractions in massive galaxies at $3 < z < 4$ (Marchesini et al. 2010). As the rest-frame *K* band is directly probed by IRAC 3.6, 4.5, 5.8, and

8 μm channels at $z \sim 0.6, 1, 1.6$, and 2.6 , respectively, the AGN-associated emission can potentially contaminate the measurements of the rest-frame K -band LFs and LDs, especially at the bright end, potentially contributing to the observed scatter in the rest-frame K -band measurements of M^* and LD. An accurate quantification of the contamination from AGN to the rest-frame K band would require a detailed modeling of the SEDs from the X-ray to the infrared associated to each object (see, e.g., Lusso et al. 2012), which is beyond the scope of this work.

5 CONCLUSIONS

In the present work, we used a composite sample constructed from deep multi-wavelength publicly available photometric catalogues from the MUSYC, FIRES and FIREWORKS survey. The availability of *Spitzer*-IRAC data in the 3.6, 4.5, 5.8, and 8 μm channels allows us to robustly estimate the LFs and LDs in the rest-frame J and H bands with a minimum dependence on the SED templates up to $z = 3.5$. Ours is the first measurement of the rest-frame H -band LF at $z > 0$ to-date. We determined the LF with three independent methods, namely the $1/V_{\text{max}}$, the SWML, and the STYML methods, finding that they agree well with each other. Uncertainties introduced by the cosmic variance were estimated using two distinct methods, one by Moster et al. (2010) and the other by Driver & Robotham (2010). We find that, for our data, the two approaches broadly agree.

Our rest-frame J -band LF is consistent with previous determination by Saracco et al. (2006), although the recovered Schechter parameters M^* and α are consistent only at the 2σ level. This might be due to the limited range in rest-frame magnitudes probed by the sample in Saracco et al. (2006) and by large errors due to cosmic variance given their small surveyed area. Our J -band LF is consistent also with the LF measured by Pozzetti et al. (2003) at $z \sim 1.5$.

We analyzed the evolution with redshift of the Schechter function parameters, making full use of the data available from the literature. We found that the faint end slope α of the LF is nearly constant over the whole redshift range, with $\alpha_J = -1.05 \pm 0.03$ and $\alpha_H = -1.15 \pm 0.02$ in the J and H bands, respectively. The characteristic density ϕ^* decreases by a factor of ≈ 6 from $z \sim 0$ to $z = 1.75$, and by a factor of ≈ 3 from $z \sim 1.75$ to $z = 3.25$. We introduced a parameterization based on an exponential form for the evolution of ϕ^* as a function of z . The fit of this function to the available data shows good agreement, especially for the rest-frame J band, where more data from the literature are available in the redshift range $z \in [0, 1]$, complementing our measurements at $z > 1.5$.

The characteristic magnitude M^* is found to brighten from $z = 0$ to $z \sim 2$ by ~ 0.8 mag, whereas M^* gets fainter with increasing redshift at $z \gtrsim 2$. We adopted a Schechter (1976)-like expression for its description, resulting in a good representation of the observed evolution.

We computed the LD in the rest-frame J and H bands, using the Schechter parameters previously determined. The LD is nearly constant up to $z \approx 1$ and decreases as a power-law by a factor of ≈ 6 from $z \approx 1$ to $z = 3.25$.

We compared the evolution with redshift of the LFs and LDs in the rest-frame J and K bands. The Schechter parameters ϕ^* and M^* in the rest-frame K band show different evolutions with redshift with respect to the J band, although these differences are only marginally significant at the 2σ level. Specifically, the decrease of

the characteristic density with redshift appears faster in the K than in the J band at $z \gtrsim 1.5$. The characteristic magnitude in the rest-frame K band brightens with redshift over the whole redshift interval $0 < z < 4$, whereas M_J^* gets brighter from $z = 0$ to $z \sim 2$, and then slowly gets fainter out to $z = 3.5$ (although a constant value of M_J^* at $z > 1.5$ is consistent within the uncertainties). Most of these differences cancel out when computing the LDs, with similar evolutions with redshift of the rest-frame J - and K -band LDs out to $z \sim 2.5$. Evidence for a faster decrease with increasing redshift of the rest-frame K -band LD at $z \gtrsim 2.5$ seems present. However, these differences are significant only to a 95% level (2σ). Large errors at $z > 2$ in both the J and K bands prevent to firmly assess differences between the evolution with redshift of the J - and K -band LFs and LDs.

In order to further constrain the rest-frame J - and H -band LFs, a larger area is needed to better probe the bright end and reduce the impact of field-to-field variations and low number statistics. Better photometric redshift estimates are also needed to improve the LF measurements at the bright end, by, e.g., reducing the impact of catastrophic outliers. The recently publicly released NEWFIRM Medium-Band Survey (Whitaker et al. 2011) will provide the dataset to significantly improve on all of these aspects. Ongoing very deep ground-based surveys, such as the UltraVISTA survey², and space-based surveys with WFC3 on the *Hubble Space Telescope*, such as the CANDELS (Grogin et al. 2011; Koekemoer et al. 2011) and 3D-HST (Brammer et al. 2011, in prep.) surveys, will allow for much improved constraints of the faint end of the rest-frame NIR LF and of the contribution of low-luminosity galaxies to the total NIR LD.

ACKNOWLEDGMENTS

We thank all the members of the FIRES, FIREWORKS, and MUSYC collaborations for their contribution to this research. We thank A. Fernandez-Soto and P. Saracco for useful comments and constructive discussions. MUSYC has greatly benefited from the support of Fundacion Andes and the Yale Astronomy Department. This work is based on observations with the *Spitzer Space Telescope*, which is operated by the Jet Propulsion Laboratory (JPL), California Institute of Technology under NASA contract 1407; based on observations with the NASA/ESA *Hubble Space Telescope*, obtained at the Space Telescope Science Institute, which is operated by AURA, Inc., under NASA contract NAS5-26555; based on observations collected at the European Southern Observatories, Chile (ESO Programme LP164.O-0612, 168.A-0485, 170.A-0788, 074.A-0709, 275.A-5060, and 171.A-3045); based on observations obtained at the Cerro Tololo Inter-American Observatory, a division of the National Optical Astronomy Observatories, which is operated by the Association of Universities for Research in Astronomy, Inc., under cooperative agreement with the National Science Foundation.

REFERENCES

- Antonucci R., 1993, ARA&A, 31, 473
- Avni Y., Bahcall J. N., 1980, ApJ, 235, 694
- Bell E. F., McIntosh D. H., Katz N., Weinberg M. D., 2003, ApJS, 149, 289

² <http://www.eso.org/sci/observing/policies/PublicSurveys/sciencePublicSurveys.html>

- Benítez N., 2000, *ApJ*, 536, 571
- Berta S., et al., 2007, *A&A*, 476, 151
- Blanton M. R., Roweis S., 2007, *AJ*, 133, 734
- Bolzonella M., Pelló R., Maccagni D., 2002, *A&A*, 395, 443
- Brammer, G. B., van Dokkum, P. G., and Coppi, P. 2008, *ApJ*, 686, 1503
- Bruzual, G., & Charlot, S. 2003, *MNRAS*, 344, 1000
- Caputi K. I., McLure R. J., Dunlop J. S., Cirasuolo M., Schael A. M., 2006, *MNRAS*, 366, 609
- Cimatti A., et al., 2002, *A&A*, 392, 395
- Cirasuolo M., et al., 2007, *MNRAS*, 380, 585
- Cirasuolo M., McLure R. J., Dunlop J. S., Almaini O., Foucaud S., Simpson C., 2010, *MNRAS*, 401, 1166
- Cole S., et al., 2001, *MNRAS*, 326, 255
- Coleman G. D., Wu C.-C., Weedman D. W., 1980, *ApJS*, 43, 393
- Conroy C., Gunn J. E., White M., 2009, *ApJ*, 699, 486
- Cowie L. L., Songaila A., Hu E. M., Cohen J. G., 1996, *AJ*, 112, 839
- Dahlen T., Mobasher B., Somerville R. S., Moustakas L. A., Dickinson M., Ferguson H. C., Giavalisco M., 2005, *ApJ*, 631, 126
- De Lucia G., Blaizot J., 2007, *MNRAS*, 375, 2
- Driver S. P., Robotham A. S. G., 2010, *MNRAS*, 407, 2131
- Drory N., Bender R., Feulner G., Hopp U., Maraston C., Snigula J., Hill G. J., 2003, *ApJ*, 595, 698
- Efstathiou G., Ellis R. S., Peterson B. A., 1988, *MNRAS*, 232, 431
- Eke V. R., Baugh C. M., Cole S., Frenk C. S., King H. M., Peacock J. A., 2005, *MNRAS*, 362, 1233
- Feulner G., Bender R., Drory N., Hopp U., Snigula J., Hill G. J., 2003, *MNRAS*, 342, 605
- Fioc, M., & Rocca-Volmerange, B. 1997, *A&A*, 326, 950
- Floyd, D. J. E., et al. 2008, *ApJS*, 177, 148
- Forster Schreiber N. et al., 2006, *AJ* 131, 1891
- Gardner J. P., Sharples R. M., Frenk C. S., Carrasco B. E., 1997, *ApJ*, 480, L99
- Gawiser, E. et al., 2006, *ApJSS*, 162, 1
- Glazebrook K., Peacock J. A., Miller L., Collins C. A., 1995, *MNRAS*, 275, 169
- Goto T., et al., 2010, *A&A*, 514, A6
- Grogin N. A., et al., 2011, *ApJS*, 197, 35
- Hill D. T., Driver S. P., Cameron E., Cross N., Liske J., Robotham A., 2010, *MNRAS*, 404, 1215
- Hönig S. F., Beckert T., Ohnaka K., Weigelt G., 2006, *A&A*, 452, 459
- Huang J.-S., Glazebrook K., Cowie L. L., Tinney C., 2003, *ApJ*, 584, 203
- Ilbert O., et al., 2006, *A&A*, 442, 423
- Inskip, K. J., Tadhunter, C. N., Morganti, R., Holt, J., Ramos Almeida, C., Dicken, D. 2010, *MNRAS*, 407, 1739
- Jones D. H., Peterson B. A., Colless M., Saunders W., 2006, *MNRAS*, 369, 25
- Kashikawa N., et al., 2003, *AJ*, 125, 53
- Kochanek C. S., et al., 2001, *ApJ*, 560, 566
- Koekemoer A. M., et al., 2011, *ApJS*, 197, 36
- Koekemoer, A. M., et al., 2011, *ApJS* submitted [arXiv:1105.375]
- Kriek M., et al., 2007, *ApJ*, 669, 776
- Labbe I. et al., 2003, *AJ* 125, 1107
- Loveday J., 2000, *MNRAS*, 312, 557
- Lusso E., et al., 2012, *arXiv*, arXiv:1206.2642
- Maraston C., 2005, *MNRAS*, 362, 799
- Marchesini D., et al., 2007, *ApJ*, 656, 42
- Marchesini D. et al., 2009, *ApJ* 701, 1765
- Marchesini D., et al., 2010, *ApJ*, 725, 1277
- Mobasher B., Sharples R. M., Ellis R. S., 1993, *MNRAS*, 263, 560
- Moster B. P., Somerville R. S., Newman J. A., Rix H.-W., 2010, *arXiv*, arXiv:1001.1737
- Pickles A. J., 1998, *PASP*, 110, 863
- Polletta M., et al., 2008, *A&A*, 492, 81
- Pozzetti L., et al., 2003, *A&A*, 402, 837
- Quadri R., et al., 2007, *AJ*, 134, 1103
- Rudnick G., et al., 2003, *ApJ*, 599, 847
- Rudnick G., et al., 2006, *ApJ*, 650, 624
- Sandage A., Tammann G. A., Yahil A., 1979, *ApJ*, 232, 352
- Saracco P., et al., 2006, *MNRAS*, 367, 349
- Schechter P., 1976, *ApJ*, 203, 297
- Schmidt M., 1968, *ApJ*, 151, 393
- Skrutskie M. F., et al., 2006, *AJ*, 131, 1163
- Szokoly G. P., Subbarao M. U., Connolly A. J., Mobasher B., 1998, *ApJ*, 492, 452
- Toft, S., et al. 2007, *ApJ*, 671, 285
- Whitaker K. E., et al., 2011, *ApJ*, 735, 86
- Wuyts, S., et al. 2007, *ApJ*, 655, 51
- Wuyts S. et al., 2008, *ApJ*, 682, 985